3.1 Introduction

Commencement of the topological insulators as a new family of quantum material initiated advanced perspectives for applications such as spintronics and quantum computing as well as for fundamental issues of quantum electrodynamics [1], [4], [90]. TIs can be described by linearly dissipated spin-polarized gap-less surface states sandwiched by the bulk band gaps. Investigation of the exotic topological properties containing new topological phases has gained enormous interest in recent years.

Raman spectroscopy is an essential non-contact method to study the optical phonon modes. This technique is believed to be complementary to spin and angle-resolved photoemission spectroscopy, providing additional and relevant information about the unique surface state of TIs [91]. Raman spectroscopy provides information about structural features, electron-phonon interactions, and inherent phonon oscillations even at very low dimensions. In the past few years, Raman spectra have been studied in conventional TIs such as Bi_2Te_3, Bi_2Se_3, Sb_2Te_3 single crystals as well as topological nano-scaled films [92]–[97]. Bi_2Te_3 exhibits Rhombohedral crystal structure and belongs to the $D_{3d}^5(R\bar{3}m)$ space group symmetry. Each unit cell of Bi_2Te_3 is constructed by five atoms forming five layers sandwiched structure [Te_1-Bi-Te_2-Bi-Te_1]. They are bonded together by van der Waals force of interaction [97]–[99]. As reported in the group theory, the phonon spectra of Bi_2Te_3 crystal consist of fifteen lattice dynamic vibrational modes. These modes are classified as three acoustic and twelve optical phonon modes. Out of all these vibrational modes, eight are detected as nondegenerate. Among those eight nondegenerate spectra, four are Raman-active (A_{1g}, E_g) and the remaining four are infrared-absorption-active (A_{1u}, E_u), which are usually mutually exclusive. The zone-center phonons can be represented as: $\Gamma = 2E_g + 2A_{1g} + 2E_u + 2A_{1u}$ [91], [92], [95], [98]–[100]. In the pump-probe experiments, apart from the excitation of the coherent transverse phonon modes, the detection of the

transverse phonon modes is much more difficult than that of the longitudinal modes. Thus, the phonon-induced anisotropy in the material should be measured to detect the transverse phonon modes [101]. Bi$_2$Te$_3$ has already been proved to have novel Raman optical properties and possess potential applications as thermoelectric devices both as bulk (3-D) and nanoscale (2-D) structure [94], [95], [97], [102]–[104]. Moreover, the rare-earth ion Dy^{3+} (4f^9) has a very high magnetic moment (10.65 μ_B) due to spin-orbit coupling[105]. Therefore, in the present work, Raman spectroscopy was studied in Bi$_{1.9}$Dy$_{0.1}$Te$_3$ to explore the surface crystal lattice dynamics and to scrutinize the influence of Dy doping on the structural and spectroscopic properties of Bi$_2$Te$_3$.

Bi$_2$Te$_3$, along with its derivative compounds, is a highly studied thermoelectric material. Such compounds and alloys are widely adopted as thermoelectric materials in solid-state cooling devices and electrical power generators operating near room temperature. Thermoelectric techniques are considered a substitution for reusing waste heat energy to solve the energy crisis and environmental issues. Thermoelectric materials are beneficial for converting waste heat directly into electricity. Such materials are believed to be one of the effective solutions to the current energy crisis [106]–[110]. The efficiency of a thermoelectric material can be determined by the power factor (PF) and figure of merit. Power factor can be estimated by the formula $PF = S^2\sigma$ and figure of merit is defined as $ZT = \frac{\sigma S^2 T}{\kappa}$, where S stands for the Seebeck coefficient, σ represents the electrical conductivity, κ implies the thermal conductivity, and T is the absolute temperature. Further, the total thermal conductivity (κ) is composed of both electronic (κ$_e$) and lattice (κ$_L$) contributions and can be derived as $\kappa = \kappa_e + \kappa_L$[111], [112]. Where κ$_e$ arises from the charge carriers and κ$_L$ emerges from the phonons. The slope of the Seebeck coefficient with temperature confirms the type of majority charge carrier present inside the material. Higher S value indicates the power factor and ZT value increment, which directly signifies the

good thermoelectric material [108], [111], [113]. To investigate the value of ZT, this is necessary to evaluate the thermal conductivity of the material. The study of temperature-dependent Raman spectroscopy is an efficient approach to investigating the value of thermal conductivity, thermal expansion properties, and inter-layer coupling of the relevant system. The temperature dependency of the Raman active peaks can be used to determine the first-order temperature coefficient by analyzing the Raman line shapes at different temperatures. From this temperature coefficient, the electronic thermal conductivity of the material can be evaluated [91], [114]. Further, the Lattice thermal conductivity (κ_L) can be evaluated in the Umklapp scattering limit [94] by employing the temperature dependency of the vibrational phonon modes. The appraised value of κ_L, along with the electronic thermal conductivity (κ_e), can be used further to calculate the total thermal conductivity (κ) as well as the figure of merit of the system [111]. In the present investigation, we have shown that $Bi_{1.9}Dy_{0.1}Te_3$ Topological insulator exhibits a large power factor and large figure of merit and verified the results by the Density functional theory calculation.

Single crystals of 5% Dy doped Bi_2Te_3 were prepared using the melt growth technique as described in section 2.2.1. X-ray powder diffraction (XRD) measurement was performed associated with Cu-K_α powder diffractometer to confirm the structure and phase of the prepared sample. The doping impact on the thermoelectric properties and thermal conductivity of the prepared sample was investigated using the thermoelectric setup in our lab. Temperature-dependent Raman spectra were recorded by 633 nm (He-Ne laser) excitation line to understand the effect of Dy doping on the structural anharmonicity and asymmetry of the system.

3.2 Result and Discussion

3.2.1 Raman Study

Pure Bi$_2$Te$_3$ exhibits rhombohedral crystal symmetry, which belongs to the space group $R\bar{3}m$ (D_{3d}^5). A primitive unit cell of pure Bi$_2$Te$_3$ accommodates two non-equivalent Te atoms formulated as Te$_1$ and Te$_2$. Two Bi atoms are bonded with Te$_1$, while Te$_2$ limits the quintuple layer. In other words, these layers are secured by van der Waals forces of interaction [104]. From symmetry consideration, the crystal lattice of the pure Bi$_2$Te$_3$ sample contains five atoms in a primitive unit cell, therefore, have fifteen lattice-driven modes at the center of the Brillouin zone at momentum $q = 0$. As described in the introduction part, optical phonon modes are distinguished as 2A$_{1g}$, 2E$_g$, 2A$_{1u}$, and 2E$_u$. Such a system acquires a center of inversion. Regulated by the crystal symmetry of the system, these optical modes are either Raman active or Infrared (IR) active. Each Raman active E$_g$ and A$_{1g}$ mode is doubly degenerated [115], [116]. The IR active E$_u$ modes are aroused by polarized electric fields that are normal to the c-axis, while the A$_{1u}$ modes are by polarized electric fields parallel to the c-axis. Considering the one-dimensional nature of A$_{1g}$ modes, the atom quivers along the (111) direction, while E$_g$ modes admitting two-dimensional nature, vibrate along normal to the (111) direction in the rhombohedral cell [101], [114]. Among the four Raman active modes, three are usually visible in Raman spectra, except for the lowest frequency E_g^1. The E_g^1 and E_g^2 modes exhibit the transverse atomic displacement, while the A_{1g}^1 and A_{1g}^2 modes demonstrate longitudinal dislocation of atoms with the c-axis [104], [117]. For pure Bi$_2$Te$_3$ single crystal, the peak frequencies of the Raman active A_{1g}^1, E_g^2 and A_{1g}^2 modes have been observed approximately at 63, 105, and 138 cm^{-1}, respectively at 300 K [30], [97], [102], [104], [118], [119]. In the present work, 5% Dy doped Bi$_2$Te$_3$ shows Raman active A_{1g}^1, E_g^2 and A_{1g}^2 modes at 59, 98 and 137 cm^{-1}, respectively at 300 K. The Raman spectra shown in Figure 3.1(a) were deconvoluted to

four peaks as 59, 98, 117, 137 cm^{-1} at room temperature, which are slightly red-shifted compared to the previously reported results [116], [119], [120]. This shifting might be caused by the rare earth magnetic Dy ion doping in the pure Bi$_2$Te$_3$ crystal. Each Raman active modes demonstrated conventional Lorentzian line shapes suppressing asymmetries. The Raman spectra of the Bi$_{1.9}$Dy$_{0.1}$Te$_3$ single crystal are shown in Figure 3.1(b) at different temperatures ranging from 100 K to 300 K. Three prominent Raman active modes are clearly detected along with an extra peak at 117 cm^{-1}. These Raman active peaks are readily identified as two A$_{1g}$ modes and one E$_g$ mode by comparing with the literature [97], [102]. Verifying the remarkable similarity of the Raman spectra between pure Bi$_2$Te$_3$ and Bi$_{1.9}$Dy$_{0.1}$Te$_3$, it can be concluded that both the Dy doped and pure Bi$_2$Te$_3$ samples share the same crystal structure. The additional peak at 117 cm^{-1} might be identified as Infrared active A_{1u}^2. But there are certain controversies behind this theory. A number of literatures have been appeared claiming that the longitudinal optical phonon mode A$_{1u}$ at wave number 117 cm^{-1} is IR active and correlated with the phonon at the zone-boundary. That might be appeared due to the lack of translational symmetry causing by a few layers of Bi$_2$Te$_3$. The IR active A$_{1u}$ modes appertain to odd parity, meanwhile, the Raman active modes E$_g$, A$_{1g}$ belong to even parity conserving inversion symmetry. However, for a few quintuple layers (FQL) the crystal symmetry often breaks along the third dimension by virtue of the restricted thickness and the existence of the interfaces. Due to such broken inversion symmetry, IR mode can be appeared in Raman spectra notwithstanding the segregated behavior of Raman and IR modes in a center symmetric crystal [97], [102], [120]. Some literature conveys IR active modes are incapable to appear in a Raman spectrum. They explained that by losing the crystal symmetry, the one-phonon density of states can be realized in a Raman scattering spectrum. In that consequence, a Raman spectrum might be disappeared caused by declination of the energy conservation. Further, the presence of

phonon modes in a Raman spectrum justifies the translational invariance in a bulk crystalline sample. Thus, the selection rules are maintained in a Raman spectrum with the existence of distinct maxima analogous to phonon vibrations. According to *C* Rodrıguez-Fernández *et al*, due to the difference in physical mechanisms, an IR active phonon frequency peak hardly can arise in a Raman measurement. They elucidated over that the excess number of Te atoms may exist in the sample initiating extra peaks in Raman spectra, as a result of the cluster formation in a Te-rich crystal [119]. Under certain consequences, the existence of additional peaks in the Raman spectra was observed in different pieces of literature. In the present work, the emergence of enormous surface properties due to rare earth doping was observed in the layered Bi$_{1.9}$Dy$_{0.1}$Te$_3$ sample [121]. The enhanced surface property and the presence of the interfaces in the layered crystal might be a reason behind the broken inversion symmetry suppressing the third dimension. In those circumstances, Infrared active A_{1u}^2 mode conceivably appeared at 117 cm^{-1} in the Raman spectra of single-crystalline Bi$_{1.9}$Dy$_{0.1}$Te$_3$.

In the temperature-dependent Raman study, with the increase in temperature A_{1g}^1, E_g^2 and A_{1g}^2 modes are shifted towards lower wavenumbers (Figure 3.1(c)), denoted as the red-shift. Single-crystalline Bi$_{1.9}$Dy$_{0.1}$Te$_3$ exhibits very large magnetoresistance (MR) (1500 % at 7 Tesla), demonstrating the surface state's robust nature. At the lowest temperature, the surface state achieves the most prominent property with the highest MR [121]. Eventually, the surface state gradually diminishes with raising the temperature, which is consistent with the red-shifted phonon modes. The first-order temperature coefficient was evaluated from the shifting of the peaks, as they exhibit a linear dependency on the temperature. The thermal expansion and contraction of the crystal and phonon modes cause anharmonicity. This anharmonicity results in the temperature-dependent peak shifting of Raman active modes between 100 K and 300 K temperature range. The value

of the temperature coefficient is comparable with the shifting of the peak. The position of

the peak centers along with the FWHM of the phonon modes were evaluated by the Raman

line shape analysis. The estimated phonon frequencies were plotted against temperature

and observed to be changed monotonically with rising temperature. These phonon

frequencies were then fitted by a linear expression,

$$\omega(T) = \omega_0 + \chi T \tag{3.1}$$

where ω_0 signifies the vibrational frequency at absolute zero temperature, χ stands for the

first order coefficient of temperature corresponding to each mode [114], [122]. The value

of the temperature coefficient for A_{1g}^1, E_g^2, A_{1u}^2 and A_{1g}^2 phonon modes were appraised as

-0.00397, -0.00334, -0.01121, and -0.00659 cm^{-1}/K, respectively (Figure 3.1(c)). This is

noticeable that the value of the first order temperature coefficients calculated for the

Bi$_{1.9}$Dy$_{0.1}$Te$_3$ single crystal is very small. Lower χ value corresponds to higher value of

figure of merit [114], which confirms Bi$_{1.9}$Dy$_{0.1}$Te$_3$ as a good thermoelectric material. Thus,

a lower value of temperature coefficients was confirmed in the single-crystalline

Bi$_{1.9}$Dy$_{0.1}$Te$_3$ adopting the temperature dependency of phonon mode frequencies [101],

[103], [114], [120]. The intensity of the Raman active vibrational phonon modes increases

with rising temperature up to 250 K (Figure 3.1(d)) which might be due to the electron-

phonon coupling interaction. The reason behind the downturn behavior above 250 K might

be the enhancement of lattice phonon vibration at higher temperatures. The FWHM of the

vibrational phonon modes has a positive linear dependency on temperature (Figure 3.1(e)).

The temperature-dependency of the peak intensity and FWHM is possibly attributed to the

zone center decaying into an optical and an acoustic phonon [101], [114]. Using the values

anticipated from the Raman line shape analysis, the first-order thermal coefficients can be

determined, which are equivalent to the thermal conductivity of the system. The area under

the curve corresponding to each Raman active mode was also determined by analyzing the

deconvoluted peaks of the Raman spectra and plotted with temperature (Figure 3.1(f)). The area under the curve and the peak intensity of each longitudinal Raman mode increase with increasing temperature up to 250 K and then decreases due to thermal scattering. The area under the curve corresponding to the transverse mode deviates from 200 K, whereas the infrared active mode increases with temperature, as shown in Figure 3.1(f).

The significance of phonon anharmonicity on the lattice thermal conductivity (κ_L) of the present Bi$_{1.9}$Dy$_{0.1}$Te$_3$ single-crystalline system can be estimated by the determination of κ_L in the Umklapp scattering limit, derived by Slack [123]. The value of κ_L used to be determined by diverse mechanisms like phonon scattering, phonon-phonon interaction and defect scattering. The Umklapp process is predominant in scattering heat conduction in phonons. The heat conduction is possible by acoustic phonons and at high temperature [94], [124]. It is essential to acknowledge the anharmonic nature of the phonon-phonon interaction in the Umklapp process. Hence, the lattice thermal conductivity was derived by Slack [123] as,

$$\kappa_L = \Lambda \frac{M\theta_D{}^3\delta}{\gamma_G{}^2 n^{2/3}T} \tag{3.2}$$

Where Λ is a physical constant $\sim 3.1 \times 10^{-6}$, *M* attributes the atomic mass average in each unit cell, which is 168.29 a.m.u. for Bi$_2$Te$_3$, δ^3 is the atomic volume $\sim$ 33.8 Å^3, *n* is the number of atoms in the primitive cell which is 5 for the present system. T denotes the corresponding temperature that is taken as 300 K [94], [125]. Debye temperature θ_D was evaluated as 157 K for Bi$_2$Te$_3$ performing specific heat measurement at D. BESSAS *et al* [125]. γ_G is denoted as the Gruneisen parameter, which identifies the appearance of the higher-order anharmonic effects near room temperature providing a detailed glimpse of the phonon dynamics and anharmonicity. Assessment of the Gruneisen parameter considering
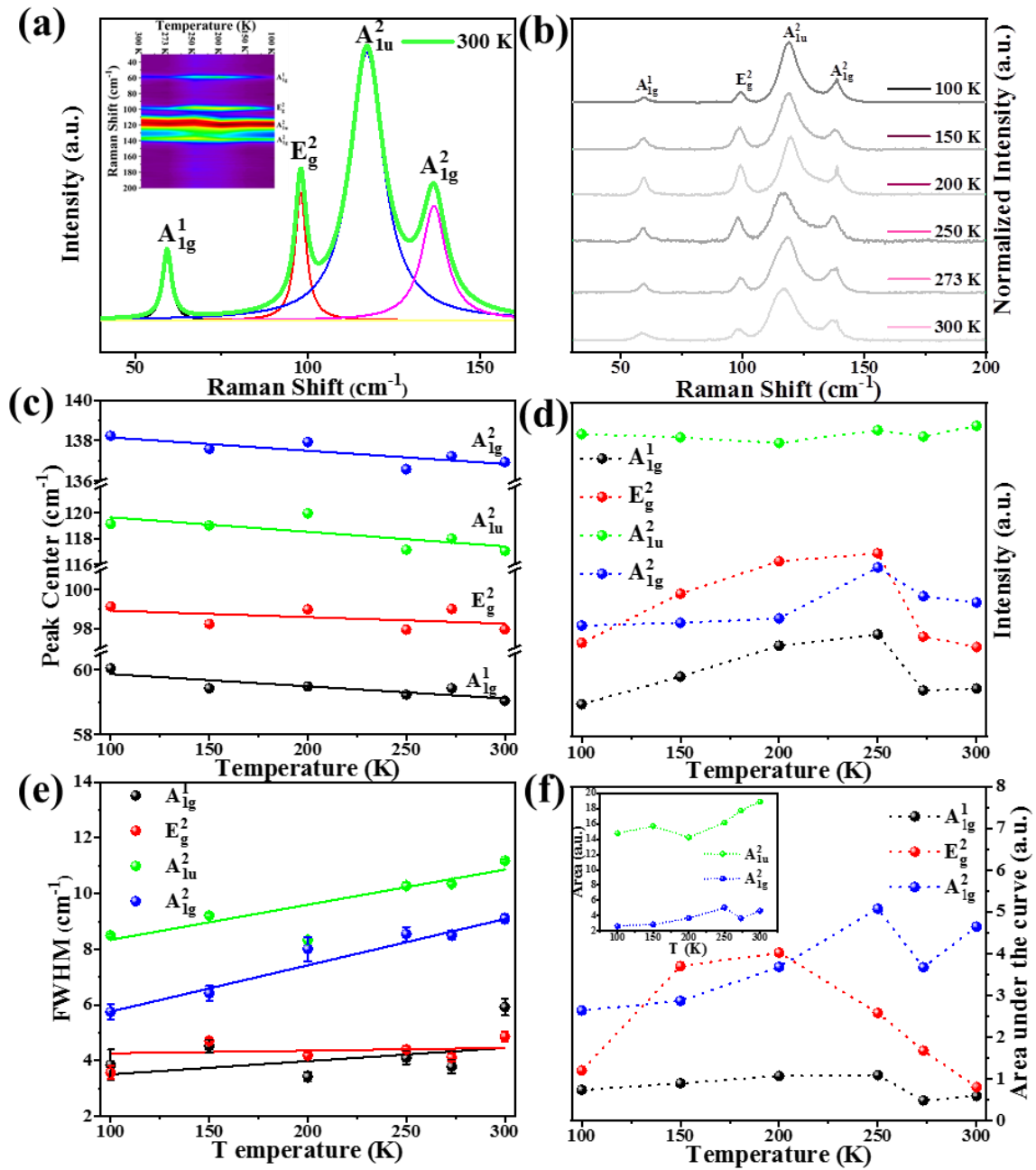
Figure 3.1: (a) Raman spectra of Single crystalline Bi$_{1.9}$Dy$_{0.1}$Te$_3$ representing the convoluted curves fitted by the Lorentzian line shape function accepting Four optical phonon mode central frequencies at 59, 98, 117, 137 cm^{-1} corresponds to A^1_{1g}, E^2_g, A^2_{1u} and A^2_{1g} optical modes at 300 K. Inset represents the projection of colour contour corresponding to the temperature-dependent Raman spectra. (b) Temperature-dependent Raman spectra exhibiting the optical phonon modes of the single crystalline Bi$_{1.9}$Dy$_{0.1}$Te$_3$ corresponding to 100 K, 150 K, 200 K, 250 K, 273 K and 300 K temperatures. (c) Peak positions of the optical phonon modes showing distinguished red-shift as a function of temperature. (d) Peak intensities of the optical modes increase with rising temperature until 250 K. (e) FWHM of Raman active optical phonon modes are linearly dependent on temperature. (f) Area under the curve of each mode differs with respect to temperature.

an anharmonic deterioration of the optical phonon modes explained the temperature-dependent Raman spectra as well as the thermal expansion parameters of $Bi_{1.9}Dy_{0.1}Te_3$ crystals. The mode value of the Gruneisen parameter illustrates the anharmonicity of the vibrational phonon mode. The anharmonic contribution in lattice thermal expansion directly corresponds to Υ_G [94], [126]. The value of Υ_G for the E_g^2 vibrational mode (frequency = 98 cm^{-1} at 300 K) in $Bi_{1.9}Dy_{0.1}Te_3$ crystal was estimated using the relation,

$\Upsilon_G = -\frac{\partial ln\,\omega}{\partial lnV}$; Where V is unit cell volume denoted as [94], $V = \frac{\sqrt{3}}{2}a^2c = 508.105$ Å^3. The lattice parameters a and c were demonstrated performing Rietveld refinement of the powder XRD data of $Bi_{1.9}Dy_{0.1}Te_3$ single crystal [127]. From the linear relation, Gruneisen parameter was calculated as 2.5898 at 300 K which is commensurate to the value of pure Bi_2Te_3 crystal [125]. Using the evaluated parameters, the lattice thermal conductivity, κ_L was estimated as 1.1095 Wm^{-1}K^{-1} for $Bi_{1.9}Dy_{0.1}Te_3$ crystal at room temperature. This value was used further to calculate the total thermal conductivity as well as the figure of merit as a thermodynamic parameter. The evaluated value of thermal conductivity is comparable to the pre-estimated value of the first order temperature coefficients. Such a low value of κ_L corresponds to the higher value of the figure of merit stands for the good thermoelectric material.

3.2.2 Thermoelectric Property

The Seebeck coefficient (S) for 5% Dy doped Bi_2Te_3 was observed to be showing a negative slope with temperature indicating the dominance of electron-like charge carriers. S value reaches 207 µV/K at room temperature (Figure 3.2). The efficiency of thermoelectric power has been determined by power factor (PF), utilizing the equation $PF = \sigma S^2$, where σ is designated as the electrical conductivity ($\sigma = 1/\rho$) (inset of Figure 3.3). The temperature reliant variation of PF for $Bi_{1.9}Dy_{0.1}Te_3$ is shown in the corner inset

of Figure 3.2. For $Bi_{1.9}Dy_{0.1}Te_3$, the value of PF reaches 5.13×10^{-3} W/K^2m at room temperature, which is much larger in comparison to those already reported for pure Bi_2Te_3 [107], [109], [128]–[130]. The enhancement of the number of conduction channels is the most probable reason behind the increment in the value of the PF due to Dy doping in Bi_2Te_3. Linear dependency of Seebeck coefficient (S) on the logarithmic value of temperature for extrinsic semiconductors conceivably described as [110],

$$S = A\frac{k_B}{e}\ln T + S_0 \tag{3.3}$$

by the foundation of Semiclassical Boltzmann Transport Theory (SCBT). S_0 represents the value of S at the absolute temperature (T = 0 K). The evaluation of the factor A in the up written equation depends on the dimensionality of the system. From the SCBT fitted statistics (Figure 3.2), the value of *A* was evaluated to be 1.63, which is consistent with the 3-D electron system. For the degenerated system like $Bi_{1.9}Dy_{0.1}Te_3$, in consequence with the semiclassical Mott Jones formula of electron transport, Seebeck coefficient can be represented as [111],[131],

$$S = \frac{8\pi^2 k_B{}^2}{3eh^2}(\frac{\pi}{3n_e})^{2/3}m^*T \tag{3.4}$$

Where m* represents the effective mass, k_B stands for the conventional Boltzmann constant, h is denoted as the Planck's constant, and n_e signifies the carrier concentration (n-type in the present system). As the Seebeck coefficient is already been demonstrated at 300 K, the carrier density (n_e) was evaluated as 3.03×10^{19} cm^{-1} by the Mott Jones formula. This value is comparable to the n_e evaluated from the hall resistivity measurement [121]. As a consequence, acquiring the n-type charge carriers, the Fermi level (E_F) should be situated near the bulk conduction band. Further, the Fermi level (E_F) was evaluated as 28.3 meV based on the Drude model for free electron gas using the equation [132],
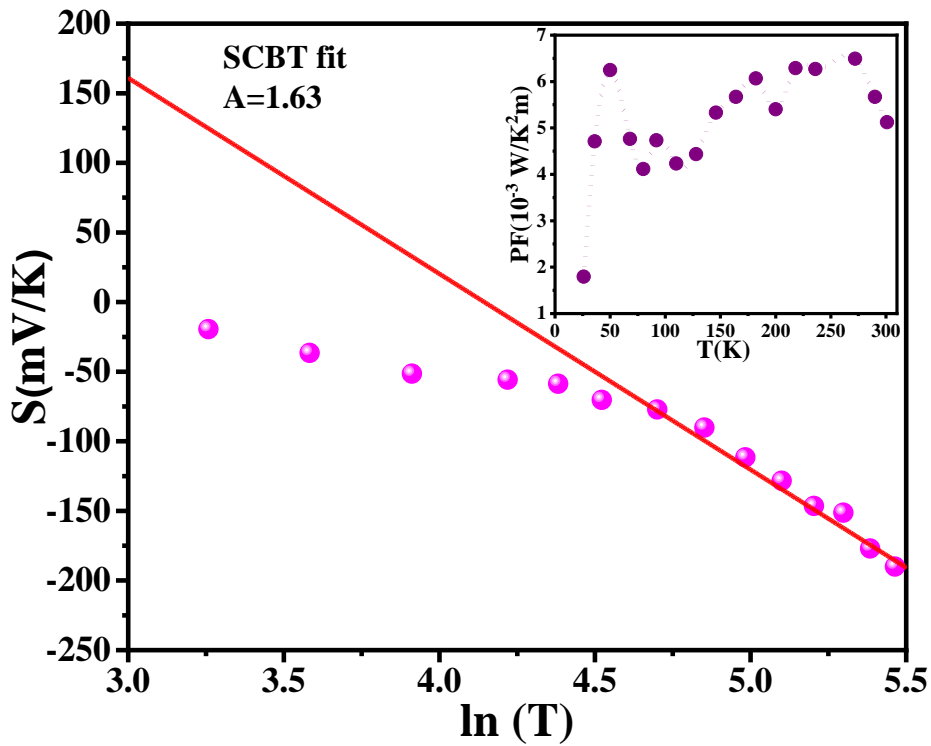
Figure 3.2: Variation of Seebeck coefficient with ln (T) is displayed in the graph where the red line represents the fitted trajectory of the Semi classical Boltzmann transport theory. Inset manifests the Power Factor of $Bi_{1.9}Dy_{0.1}Te_3$ as the temperature variance.
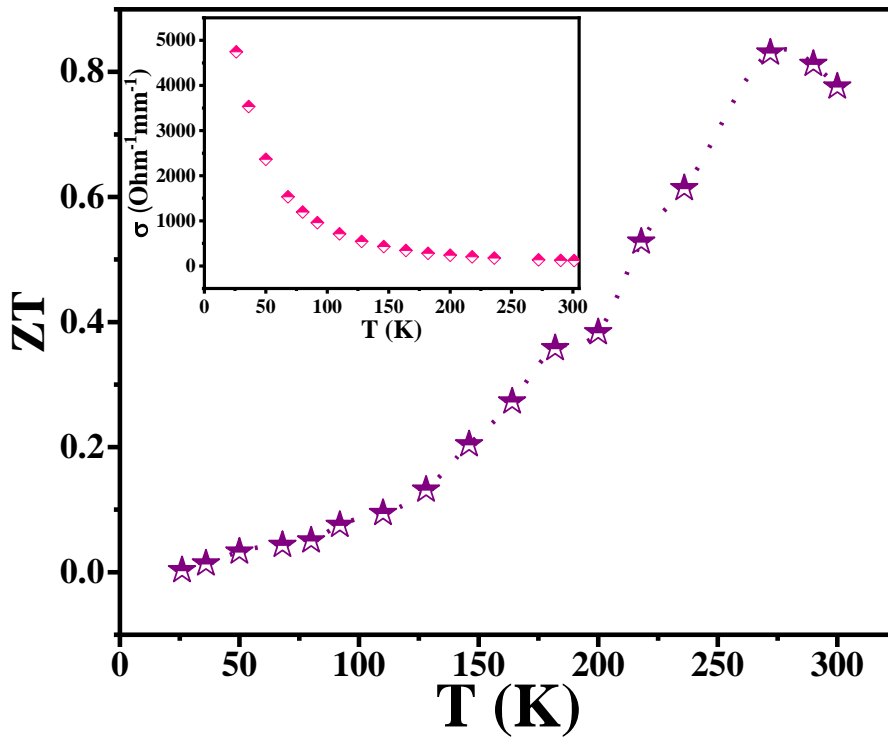

Figure 3.3: The calculated values of the figure of merit are represented with respect to temperature. Inset shows the variation of electrical conductivity with temperature.

$$S = \frac{\pi^2 k_B{}^2 T}{6 e E_F} \tag{3.5}$$

According to the vibrational phonon study, the reduction of temperature coefficient was confirmed with the increase in temperature. With a greater value of S and a smaller value of the thermal coefficient, the figure of merit enhances, denoting the single crystalline $Bi_{1.9}Dy_{0.1}Te_3$ as a better thermoelectric material. The total thermal conductivity incorporates the electronic κ_e and lattice κ_L contribution as $\kappa = \kappa_e + \kappa_L$. The electronic contribution of the thermal conductivity was anticipated by the Wiedemann–Franz law [23,24,46]:

$$\kappa_e(T) = LT\sigma \tag{3.6}$$

where L is denoted as Lorentz number and σ stands for the electrical conductivity. L is treated as a universal factor with value 2.44×10^{-8} $W\Omega K^{-2}$ (degenerate limit), which can be demonstrated from the measured S(T) data. Thus, $\kappa_e(T)$ was evaluated as 0.8709 $Wm^{-1}K^{-1}$ for $Bi_{1.9}Dy_{0.1}Te_3$ adopting the estimated values of L and measured resistivity ($\rho(T)$) value at 300 K. Figure 3.4 represents the electronic contribution of thermal conductivity varies with raising temperature. This electronic contribution was realized mainly due to the metallic surface state of the present TI. Using the evaluated parameters by the Umklapp process, the lattice thermal conductivity, κ_L was determined as 1.1095$Wm^{-1}K^{-1}$ for $Bi_{1.9}Dy_{0.1}Te_3$ crystal at room temperature. According to the Wiedemann-Franz law, the evaluated values of κ_L and κ_e confirmed that the lattice thermal conductivity dominates over the electronic thermal conductivity [112] (Figure 3.4). This justifies the idea that the insulating bulk plays an important role in the thermoelectric property of the system. Accepting the values of κ_L and $\kappa_{e,}$ the total thermal conductivity (κ) (Figure 3.4) for $Bi_{1.9}Dy_{0.1}Te_3$ was determined as 1.9804 $Wm^{-1}K^{-1}$. We have also measured the thermal conductivity at room temperature using the steady state method. The obtained value

$(2.17765 \ Wm^{-1}K^{-1})$ is consistent with the estimated thermal conductivity value (mentioned above). From the fitted values of magneto conductivity, the contribution of the electron-electron and electron-phonon interactions were calculated as $A_{ee} = -163.44 \ nm^{-2}$ and $A_{ep} = -0.19 \ nm^{-2}$, respectively. Electron-phonon interaction plays a crucial character in electrical conductivity, adjusting both the lifetime and the dispersion relation of electron and phonon states [134]. The dominating electron-electron interaction contributes to the thermal conductivity of the material. Further, using the estimated values of the thermal conductivity (κ) and the electrical conductivity (σ) at room temperature (300 K), the figure of merit was calculated as $ZT = \frac{\sigma S^2 T}{\kappa} = 0.7764$ (Figure 3.3). On the other hand, using the value of thermal conductivity measured by steady state method figure of merit was evaluated as 0.7061 which is consistent with the estimated ZT value (0.7764). The obtained value of figure of merit is certainly a high value to be reported confirming Bi$_{1.9}$Dy$_{0.1}$Te$_3$ acquires a good thermoelectric property.
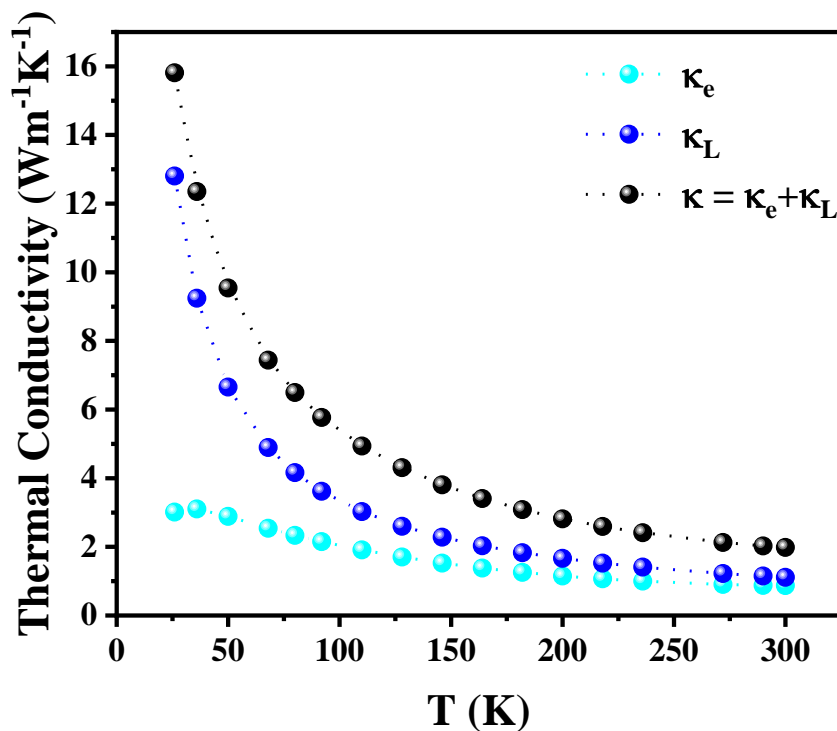

Figure 3.4: Electronic and lattice contribution of thermal conductivity as well as the total thermal conductivity is plotted against Temperature.

3.2.3 Theoretical Analysis

In order to further understand the effect of Dy doping in Bi$_2$Te$_3$, which results in a large power factor and figure of merit value, we have performed spin-polarized calculation within the framework of density functional theory (DFT) [135] using the Vienna ab-initio simulation package (VASP) [136]. The Perdew-Bruke-Ernzerhof generalized gradient approximation (PBE-GGA) [137] is used as exchange-correlation functional, and the core and valence interaction effects are included in terms of the projector-augmented-wave (PAW) method. We consider Dy (6s, 4f), Bi (6s, 6p) and Te (5s, 5p) as valence electrons, while other states are assumed as core electrons. Plane-wave basis sets are used with an energy cut-off equal to 350 eV. High energy convergence criteria (10^{-6} eV) are used for all sets of calculations. The Brillouin zone (BZ) integration for conventional cell (supercell) was performed at 8×8×8 (6×6×1) Monkhorst-Pack [138] k-points mesh by adopting a conjugate gradient scheme. The residual Hellman-Feynman force on atoms reduced up to ≤ 0.01 eV/Å. We are using experimentally measured lattice constants (a=b=4.386(8) Å, c=30.499(5) Å) for the pure Bi$_2$Te$_3$ system. However, to dope Dy atoms into Bi$_2$Te$_3$ lattice, a supercell of size 2×1×2 was generated. The structure optimization in the form of relaxation of the atomic position shows that the neighbouring atoms of Dy move towards and accommodate with smaller Dy-Te bond length, but the atoms far from Dy show a minute change in Dy-Te bond length and maintain its crystal structure. The change in bond length between Dy-Te varied from 0.01 to 0.1 Å with respect to Bi-Te. The electronic properties of the Dy-doped system were studied for supercell of size $2 \times 1 \times 2$ consisting of six Quintuple layers (QLs), as shown in Figure 3.5(a). The calculation has been made by considering the spin-orbit coupling. It has been established that the use of GGA functional into calculation of electronic structure of a material may severely underestimate energy band gap of a material. Therefore, to overcome this difficulty we adopt GGA+U

[139] approach and shifted the *f* orbital of Dy by taking into consideration the Hubbard term U = 7.0 eV [140], which matches our experimental results well. Further, to unearth the underlying physics, we have performed systematic studies of electronic band structure and electronic density of states of pristine and Dy doped Bi_2Te_3 and compared the role of spin-orbit coupling (SOC) in band splitting. The calculated band structures of pure Bi_2Te_3 in a hexagonal lattice with and without SOC have been illustrated in Figure 3.5(b). From Figure 3.5(c), it is clear that the SOC effect strongly dominated in the material, and drastic change originated in valence and conduction band edge while moving for Γ to M direction in Brillouin zone. However, without SOC calculations, both the valence and conduction band edges lie at Γ and renders the material as direct energy band gap of 0.29 eV. On the other hand, after including SOC, results show that the energy band gap of the materials changes from direct to indirect energy band gap may be due to shifting of valence and conduction band edges (Figure 3.5(c)). Thus, for the study of $Dy_2Bi_{22}Te_{36}$ system, we have intentionally incorporated SOC effect while calculating the band structure. The calculated band structure for $Dy_2Bi_{22}Te_{36}$ system is depicted in Figure 3.5(d). It is evident that the separation between valence and conduction band minimum (CBM) at Γ is ∼ 55 meV, which supports our experimental result. This reduced bang gap clearly indicates that the doping of Dy into Bi_2Te_3 enhances metallic character. It will be interesting to know the band character responsible for introducing the metallic property in $Dy_2Bi_{22}Te_{36}$.

Thus, charge carrier density increases by introducing Dy ion in Bi_2Te_3. Conductivity displays linear relation with the PF and ZT of the system. This is established experimentally that Dy doping enhances the PF (5.13×10^{-3} W/K²m) and ZT (0.7764) values presenting $Bi_{1.9}Dy_{0.1}Te_3$ as a better thermoelectric material. To get deep insight into the electronic structure, we now concentrate our attention on predicting hybridization between different atomic orbitals. For that purpose, we have calculated the projected density of

states (PDOS), as presented in Figure 3.5(e). Looking to PDOS for the bulk system, it is clear that both valence and conduction band edges are formed by strong hybridization of Bi-p and Te-p orbitals. The contribution of Dy-*f* orbitals appears around 0.5 eV above the Fermi energy level.
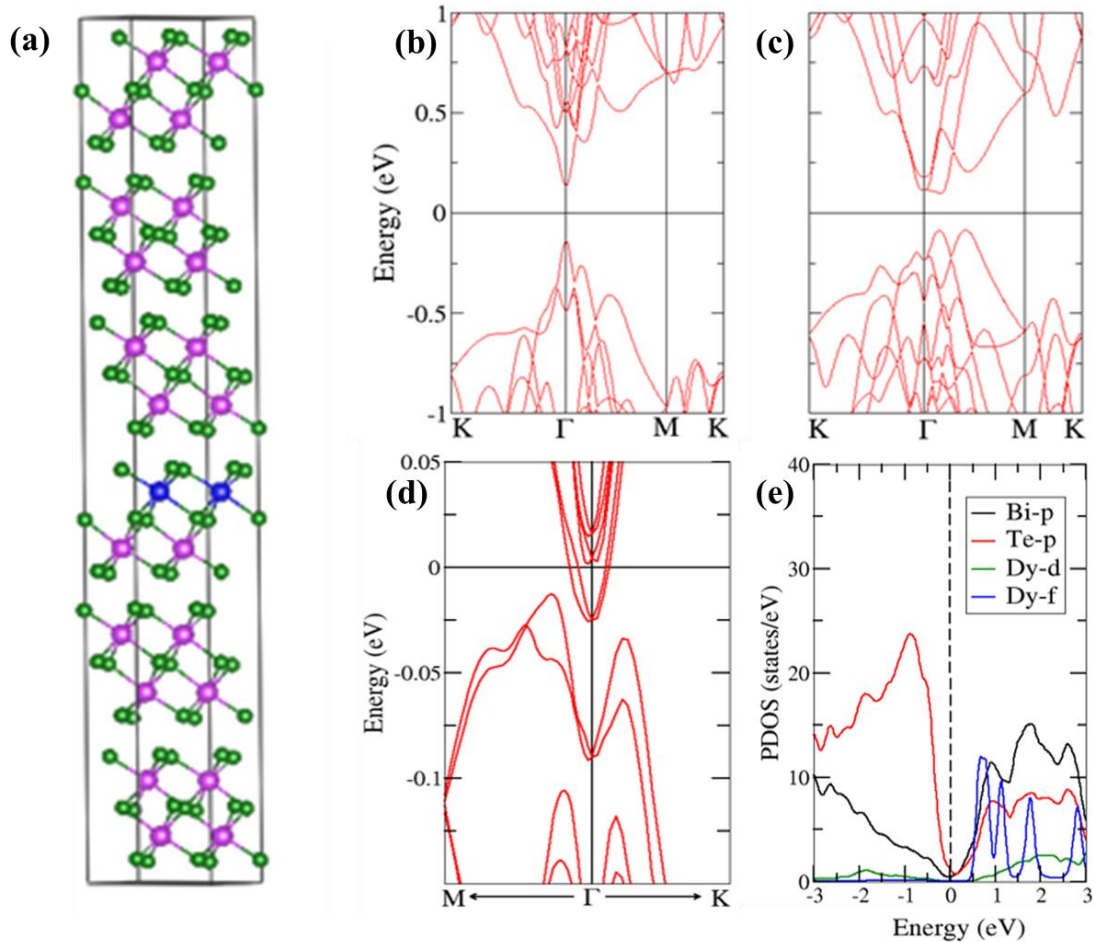

Figure 3.5: (a) The optimized cell of Dy$_2$Bi$_{22}$Te$_{36}$ of size 2×1×2 in hexagonal lattice where Dy (blue), Bi (magenta) and Te (green) atoms are represented by filled solid sphere, (b) band structure of pure Bi$_2$Te$_3$ calculated without SOC and (c) with SOC effect. The band structure and PDOS of Dy$_2$Bi2Te$_3$ are presented in (d) and (e), respectively (calculated with SOC).

3.3 Conclusion

The temperature dependency of the phonon dynamics in the Bi$_{1.9}$Dy$_{0.1}$Te$_3$ sample is readily described by the anharmonicity of phonon-phonon interaction, indicating a dominant surface state. Temperature-dependent Raman spectra demonstrated the red-shift of Raman modes and broadening of FWHM with increasing the temperature from 100 K

to 300 K. Linear temperature dependency of the vibrational phonon modes of Bi$_{1.9}$Dy$_{0.1}$Te$_3$ was revealed. Thermoelectric measurement proved the higher value of the Seebeck coefficient (207 μV/K at 300 K) as well as an enlarged power factor (5.13×10^{-3} W/K^{2}m). Using the Umklapp method, the lattice contribution of thermal conductivity was determined as 1.1095 Wm^{-1}K^{-1} estimating the anharmonic Gruneisen parameter. The electronic contribution of thermal conductivity was estimated as 0.8709 Wm^{-1}K^{-1} employing the Wiedemann–Franz law. The total thermal conductivity was determined by adding both the lattice and electronic contributions and was proven to be comparable with the measured thermal conductivity value at room temperature. Further, the figure of merit was evaluated as 0.7764 using the values of Seebeck coefficient, thermal conductivity and electrical conductivity at room temperature. The large power factor and Figure of merit have been supported by DFT calculation. This is noteworthy to mention that the single crystalline Bi$_{1.9}$Dy$_{0.1}$Te$_3$ demonstrates the possibility of being used as an excellent thermoelectric material. Better quality crystals along with large-scale production obtaining high performance, will push its application in the field of better thermoelectric materials. The main findings in this work will be beneficial to future thermoelectric and electronic applications.